Surface controlled reduction kinetics of nominally undoped polycrystalline CeO_2

Nicole Knoblauch,[a] Lars Dörrer,[b] Peter Fielitz,*[b] Martin Schmücker[a] and Günter Borchardt[b]

Ceria is an interesting material for high temperature redox applications like solar-thermal splitting of CO_2 and H_2O. Technical implementation and reactor design for solar-thermal redox-based fuel generation requires reliable data for the chemical surface exchange coefficient and the chemical diffusivity of oxygen. The results of thermogravimetric relaxation experiments and equilibrium oxygen isotope exchange experiments with subsequent depth profiling analysis suggest that the reduction reaction of even dense samples of pure ceria (1 mm thickness, 93% of theoretical density) with a grain size of about 20 µm is surface reaction controlled. The chemical surface exchange coefficient exhibits a negative apparent activation energy (-64 kJ mol^{-1}). This finding is corroborated by similar data from literature for the tracer surface exchange coefficient. The structure of the derived expression for the apparent activation energy further suggests that the chemical surface exchange coefficient should show only a very weak dependence on temperature for ceria doped with lower valence cations.
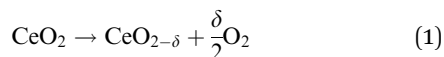
1 Introduction

Non-stoichiometric ceria is a promising redox material for water and CO_2 splitting not only because of suitable thermodynamics but also because of beneficial reaction kinetics. The H_2O/CO_2-splitting cycle consists of two thermochemical reactions,[1] a high-temperature reduction step

$$CeO_2 \rightarrow CeO_{2-\delta} + \frac{\delta}{2}O_2 \qquad (1)$$

and a low-temperature re-oxidation step going along with the splitting of water or CO_2

$$CeO_{2-\delta} + \delta H_2O(g) \rightarrow CeO_2 + \delta H_2(g) \qquad (2a)$$

$$CeO_{2-\delta} + \delta CO_2(g) \rightarrow CeO_2 + \delta CO(g) \qquad (2b)$$

Reduction of CeO_2 occurs at elevated temperatures and/or low oxygen partial pressure by the formation of oxygen vacancies as a consequence of gradual oxygen release. Resulting non-stoichiometric ceria is characterized by the suboxide parameter δ determined by applied T/p_{O_2} conditions (1). Subsequent re-oxidation of $CeO_{2-\delta}$ in the presence of H_2O and/or CO_2 according to eqn (2a) and (b) causes H_2O/CO_2 splitting and hence H_2 and/or CO release.

A deeper insight into mechanisms and kinetics of ceria reduction and re-oxidation is required in view of future technical realization.

In general, redox kinetics of ceria is either controlled by surface exchange reactions or by bulk transport of oxygen. Previous studies of the reaction kinetics comprise oxygen isotope exchange in chemical equilibrium and relaxation experiments based on oxygen potential changes. Depending on the microstructure of the sample material used in the different studies, the respective authors derived surface exchange coefficients, K, or diffusivities, D, of oxygen, or both of them.[2–10] There is also comprehensive literature on the general relation between the tracer parameters, $K^\star$ and $D^\star$, and the corresponding chemical parameters, $\tilde{K}$ and $\tilde{D}$ (see, *e.g.*, Maier[11] and references therein) or on the tracer surface exchange coefficient, $K^\star$ (see, *e.g.* De Souza,[12] Armstrong *et al.*[13]), which evoke, however, some controversies as to the meaning of the obtained parameters, especially with respect to the transport regime characterized by a characteristic thickness $l_c = D/K$.[14] Especially *chemical* relaxation experiments are sometimes difficult to categorize with respect to the reaction regime as both $\tilde{K}$ and $\tilde{D}$ depend on the oxygen activity (which changes with time during the experiment).

Further, due to the high (chemical) diffusivity of oxygen in nominally undoped (as well as in appropriately doped) ceria the surface exchange regime should not be excluded a priori even for fairly dense samples ($>90\%$ of theoretical density) for the high temperature reduction step. This position will be elaborated in the following section for both the reduction and the (re)oxidation step simultaneously as the phenomenological treatment is the same. The conclusions will then be applied in Sections 3 and 4 to the reduction step of a prototype *chemical* relaxation experiment (thermogravimetric analysis, TGA) in

[a] *Deutsches Zentrum für Luft- und Raumfahrt, Institut für Werkstoff-Forschung, Linder Höhe, D-51147 Köln, Germany*

[b] *Technische Universität Clausthal, Institut für Metallurgie, Robert-Koch-Str. 42, D-38678 Clausthal-Zellerfeld, Germany. E-mail: peter.fielitz@tu-clausthal.de*

This journal is © the Owner Societies 2015

Phys. Chem. Chem. Phys., 2015, **17**, 5849–5860 | 5849

Paper

PCCP

combination with a prototype *equilibrium* tracer isotope exchange experiment. The interpretation of the data will partially rely on supporting evidence from the literature.

2 Mathematical modelling

In this section we will mathematically model the kinetics of reduction–oxidation processes of solid oxides in a narrow oxygen potential range. For that, we assume, in a first approximation, that it is sufficient to model the reduction–oxidation process by two constant parameters $\tilde{D}$ and $\tilde{K}$ which depend only on temperature, where $\tilde{D}$ is an effective chemical oxygen diffusion coefficient and $\tilde{K}$ an effective chemical surface exchange coefficient of oxygen at the gas/solid interface. For convenience we simply refer in this chapter to $\tilde{D}$ as oxygen diffusion coefficient and to $\tilde{K}$ as surface exchange coefficient of oxygen and we use in the equations (D,K) instead of $(\tilde{D},\tilde{K})$. The advantage of such a simple model is that it allows one to derive analytical solutions which yield significant insight into the role the microstructure of a given material has on the overall kinetics of the reduction–oxidation process.

2.1 Reduction–oxidation kinetics of a sphere

Reduction–oxidation experiments are often performed with powders, which are characterised by an average diameter of the powder particles, so that it is useful to model the reduction–oxidation kinetics of a sphere of radius R. Solving the diffusion equation in the case of radial diffusion and constant diffusion coefficient, D, and considering a constant oxygen surface exchange coefficient, K, at the gas/solid interface the relative mass change of a sphere during the reduction–oxidation process is given by Crank[15] (p. 96)

$$\left|\frac{m(t)-m_0}{m_\infty-m_0}\right|_{\text{sphere}} = 1 - \sum_{n=1}^{\infty}\frac{6L^2\exp\left(-\beta_n^2 Dt/R^2\right)}{\beta_n^2(\beta_n^2+L^2-L)}$$

$$\text{with}\quad L \equiv R\frac{K}{D} \tag{3}$$

where m_0 is the mass of the sample at time $t = 0$, m_∞ is the (equilibrium) mass of the sample at time $t = \infty$. The values of the dimensionless parameter β_n are positive roots of $\beta_n \cot \beta_n = 1 - L$. The first six roots are tabulated by Carslaw and Jaeger[16] (p. 492). The infinite sum in eqn (3) converges rapidly[17] so that it is practically sufficient to consider the first term of eqn (3)

$$\left|\frac{m(t)-m_0}{m_\infty-m_0}\right|_{\text{sphere}} \simeq 1 - \frac{6L^2\exp\left(-\beta_1^2 Dt/R^2\right)}{\beta_1^2(\beta_1^2+L^2-L)}$$

$$\text{with}\quad \beta_1 \cot \beta_1 = 1 - L \tag{4}$$

The characteristic time constant of the relative mass change of the sphere is, therefore, given by

$$(\tau_1)_{\text{sphere}} = \frac{1}{\beta_1^2}\frac{R^2}{D} \tag{5}$$

where R is the radius of the solid sphere, D is the oxygen diffusion coefficient in the solid and the dimensionless β_1 value is the first positive root of $\beta_n \cot \beta_n = 1 - L$. See Fig. 1 to get an impression how the term $1/\beta_1^2$ of eqn (5) depends on $L = RK/D$.
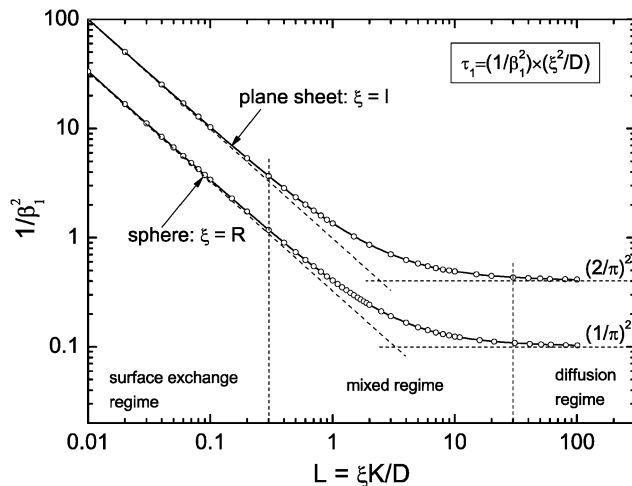

Fig. 1 Graphical representation of the term $1/\beta_1^2$ of eqn (5) or (10), respectively. Open points are first roots of $\beta_n \cot \beta_n = 1 - L$ and $\beta_n \tan \beta_n = L$, respectively, which are tabulated by Carslaw and Jaeger[16] (pp. 491–492).

From Fig. 1 one gets the approximation $\beta_1^2 \simeq 3L$ for values $L < 0.3$ (see also Appendix A) so that eqn (4) and (5) simplify

$$\left|\frac{m(t)-m_0}{m_\infty-m_0}\right|_{\text{sphere}}^{K\,\text{regime}} \simeq 1 - \exp\left(-\frac{t}{\tau_1}\right)$$

$$\text{with}\quad \tau_1 = \frac{R}{3K}\quad \text{if}\quad D > 3RK \tag{6}$$

This equation describes the kinetics of the surface exchange regime which is controlled by the surface exchange coefficient, K, of oxygen. This regime is generally reached if the radius of the grains becomes sufficiently small. The factor 3 in the condition $D > 3RK$ was graphically estimated (see $L = RK/D < 0.3$ in Fig. 1).

In the mixed regime (see $0.3 \leq L \leq 30$ in Fig. 1) the observed kinetics of the reduction–oxidation process is influenced by contributions of both parameters K and D. For sufficiently large spheres the dimensionless parameter L in Fig. 1 becomes sufficiently large (at about $L > 30$) so that one has $\beta_1^2 \simeq \pi^2$. In this case eqn (4) and (5) simplify

$$\left|\frac{m(t)-m_0}{m_\infty-m_0}\right|_{\text{sphere}}^{D\,\text{regime}} \simeq 1 - \frac{6}{\pi^2}\exp\left(-\frac{t}{\tau_1}\right)$$

$$\text{with}\quad \tau_1 = \frac{R^2}{\pi^2 D}\quad \text{if}\quad D < \frac{RK}{30} \tag{7}$$

In contrast to eqn (6) this approximation will become inadequate for very short times (one gets $1-6/\pi^2 = 0.39$ instead of zero for $t = 0$). However, as demonstrated in Section 2.3, eqn (7) will be practically applicable if one monitors the time dependence of the reduction–oxidation process up to equilibrium (practically at $t > 5\cdot\tau_1$).

2.2 Reduction–oxidation kinetics of a plane sheet

We now consider a plane sheet of thickness $h = 2l$ in which oxygen can leave/penetrate both surfaces in the reduction–oxidation step. This geometry is often a good approximation if powder is pressed and then sintered to dense samples. Solving the diffusion

5850 | *Phys. Chem. Chem. Phys.*, 2015, **17**, 5849–5860

This journal is © the Owner Societies 2015

equation in the case of one-dimensional diffusion and constant diffusion coefficient, D, and considering a constant oxygen surface exchange coefficient, K, at the gas/solid interface one obtains for the relative mass change of a plane sheet during the reduction–oxidation process (Crank[15] p. 60)

$$\left|\frac{m(t) - m_0}{m_\infty - m_0}\right|_{\text{plane sheet}} = 1 - \sum_{n=1}^{\infty} \frac{2L^2 \exp\left(-\beta_n^2 Dt/l^2\right)}{\beta_n^2 (\beta_n^2 + L^2 + L)} \tag{8}$$

$$\text{with} \quad L \equiv l\frac{K}{D}$$

where m_0 is the mass of the sample at time $t = 0$, m_∞ is the (equilibrium) mass of the sample at time $t = \infty$. The dimensionless β_n values are positive roots of $\beta_n \tan \beta_n = L$ where l is half the thickness of the plane sheet. The infinite sum in eqn (8) converges rapidly[17,18] so that eqn (8) can be approximated by

$$\left|\frac{m(t) - m_0}{m_\infty - m_0}\right|_{\text{plane sheet}} \simeq 1 - \frac{2L^2 \exp\left(-\beta_1^2 Dt/l^2\right)}{\beta_1^2 (\beta_1^2 + L^2 + L)} \tag{9}$$

$$\text{with} \quad \beta_1 \tan \beta_1 = L$$

That is, a characteristic time constant of the relative mass change of a plane sheet is given by

$$(\tau_1)_{\text{plane sheet}} = \frac{1}{\beta_1^2}\frac{l^2}{D} \tag{10}$$

A graphical representation of the term $1/\beta_1^2$ of eqn (10) is presented in Fig. 1. Analogous to the discussion in Section 2.1 one can consider the surface exchange regime which is practically reached for values $L < 0.3$ so that one has the simple relation $\beta_1 \simeq L$ (see also Appendix A). In this case eqn (9) and (10) simplify

$$\left|\frac{m(t) - m_0}{m_\infty - m_0}\right|_{\text{plane sheet}}^{K\,\text{regime}} \simeq 1 - \exp\left(-\frac{t}{\tau_1}\right) \tag{11}$$

$$\text{with} \quad \tau_1 \simeq \frac{l}{K} \quad \text{if} \quad D > 3l/K$$

The surface exchange controlled regime is generally reached for sufficiently thin sheets. For sufficiently thick sheets the

diffusion controlled regime in Fig. 1 is reached (at about $L > 30$) so that one has $\beta_1^2 \simeq \pi^2/4$. In the diffusion controlled regime eqn (9) simplifies

$$\left|\frac{m(t) - m_0}{m_\infty - m_0}\right|_{\text{plane sheet}}^{D\,\text{regime}} \simeq 1 - \frac{8}{\pi^2}\exp\left(-\frac{t}{\tau_1}\right) \tag{12}$$

$$\text{with} \quad \tau_1 \simeq \frac{4}{\pi^2}\frac{l^2}{D} \quad \text{if} \quad D < \frac{lK}{30}$$

where $l = h/2$ is half the thickness of the plane sheet. As discussed above (see discussion related to eqn (7)) this approximate solution of the diffusion controlled regime does not work for very short times ($t \ll \tau_1$) so that we will discuss the correct application of the approximate solutions in the next section.

2.3 Application of the approximate solutions as fit equations

To test the accuracy of the approximate equations we calculated the normalized mass change data with the aid of the exact eqn (3) and (8) using Maple software (Waterloo Maple Inc., Canada). For that the first six roots of $\beta_n \tan \beta_n = L$ and $\beta_n \cot \beta_n = 1 - L$ were used which are tabulated by Carslaw and Jaeger[16] (p. 491–492). The calculated data were then fitted by Origin software (OriginLab Inc., USA) using this fit equation

$$y = y_0 + A_1 \exp\left(-\frac{x - x_0}{t_1}\right) \tag{13}$$

which is a standard fit equation (ExpDecay1) in Origin software. Comparing this fit equation with the approximate eqn (6), (7), (11) and (12) one sees that A_1 must be negative and one must fix the fit parameters $y_0 = 1$ and $x_0 = 0$.

As discussed above (see remarks related to eqn (7)) one can conclude that in the diffusion controlled regime the approximate solutions will not work for very short times ($t \ll \tau_1$). However, in this paper we discuss the kinetics of a reduction–oxidation process which is typically monitored until equilibrium is reached. In Fig. 2 we tested the approximate solution (fit eqn (13)) for this case. If one simply fits eqn (13) to the complete calculated data set one can expect an error of the
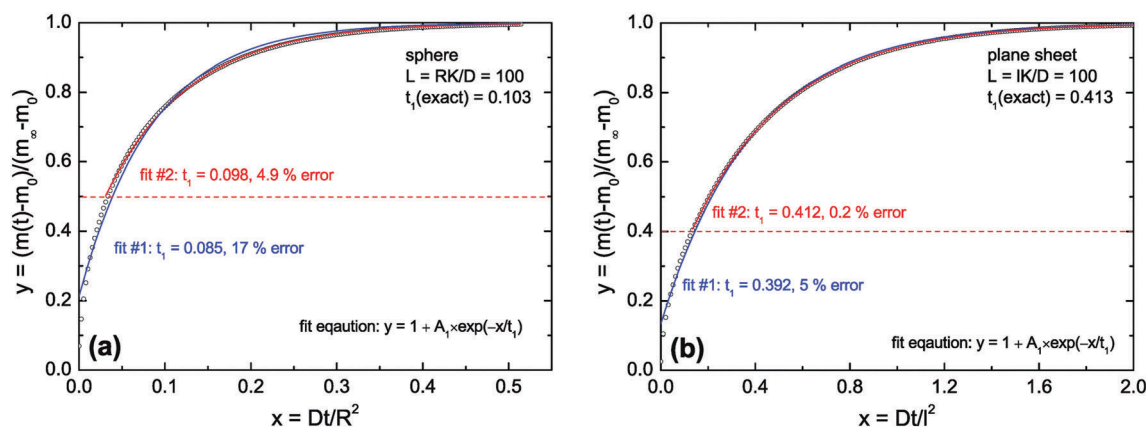

Fig. 2 Open points are calculated values for $L = 100$ (diffusion controlled regime). In (a) eqn (3) was used and in (b) eqn (8) was used (the first six roots in both cases). Fit #1: The complete set of calculated data was fitted by eqn (13). Fit #2: All calculated data in the range $0 \le y \le y_{\text{start}}$ were excluded from the fitting procedure, with $y_{\text{start}} = 0.5$ in the case of a sphere (a) and $y_{\text{start}} = 0.4$ in the case of a plane sheet (b).
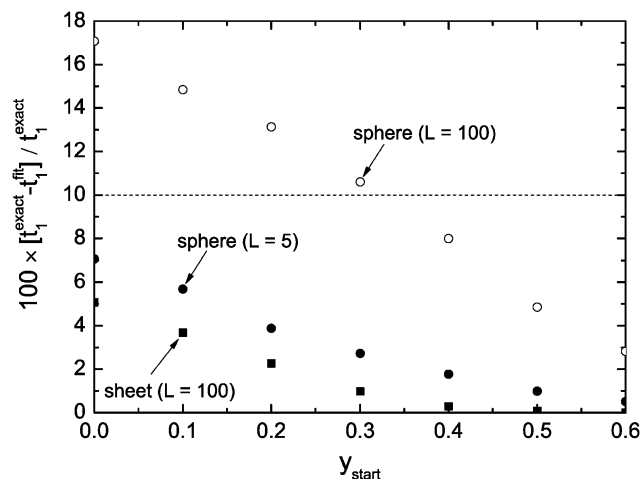
This journal is © the Owner Societies 2015

Phys. Chem. Chem. Phys., 2015, **17**, 5849–5860 | 5851

Fig. 3 Percentage error of the evaluated time constants, t_1, if one excludes the range $0 \leq y \leq y_{\text{start}}$ from the fitting procedure.

evaluated time constant of about 17% in the case of the sphere and about 5% in the case of the plane sheet. However, if one excludes short time data one gets significantly more accurate fit values for the time constants. In Fig. 2a (sphere) all data in the range $0 \leq y \leq y_{\text{start}} = 0.5$ were excluded during a second fitting procedure. One can see that the fit becomes significantly better now and that the error of the evaluated time constant is reduced to about 5% which is practically acceptable. The same strategy (excluding short time data from the fitting procedure) leads in the case of a plane sheet even to an accuracy of 0.2% (see fit #2 in Fig. 2b).

Fig. 3 shows the dependence of the error of the evaluated time constant if the range $0 \leq y \leq y_{\text{start}}$ is excluded during the fitting procedure. One can see that one gets in the case of a plane sheet very accurate time constants if one excludes the data range $0 \leq y \leq y_{\text{start}} = 0.3$ from fitting. However, in the case of a sphere the same strategy leads to an error of about 10%. To reduce the error to about 5% one must exclude the data range $0 \leq y \leq y_{\text{start}} = 0.5$ from the fitting procedure. One could argue that this result makes the discussed approximate solutions unusable for spheres. However, one has to keep in mind that we consider typically spheres of microscopic dimensions where one can expect lower values than $L = 100$ (diffusion controlled regime). Fig. 3 shows that in the mixed regime ($L = 5$) the accuracy is about 3% if one excludes the data range $0 \leq y \leq y_{\text{start}} = 0.3$ from fitting. That is, the exclusion of short time data from the fitting procedure with fit eqn (13) is generally a good strategy to evaluate time constants with practically sufficient accuracy.

2.4 Reduction–oxidation kinetics of polycrystalline solids in the A regime

Powders are pressed into any desired form to produce macroscopic bodies and then sintered at high temperatures to polycrystalline solids. The oxygen transport, and hence, the reduction–oxidation kinetics, of a polycrystalline solid is influenced at least by 4 parameters: In the single crystalline grains of average radius R oxygen is transported with the bulk diffusivity D. In the grain

boundaries oxygen is typically transported significantly faster with the grain boundary diffusivity D_{gb}. The average width of the grain boundaries is taken into account by the parameter ω.

The mathematical treatment of grain boundary diffusion is described comprehensively by Kaur et al.[19] In the A regime mathematical modelling is significantly simplified because a polycrystalline solid behaves in this regime like a homogeneous medium with some effective diffusivity, D_{eff}, which is given by the Hart–Mortlock equation[20,21]

$$D_{\text{eff}} = sgD_{\text{gb}} + (1 - sg)D \qquad (14)$$

where $g \approx q\omega/(2R)$ is the volume fraction of grain boundaries and q a geometrical factor. For cubic grains one gets $q \approx 3$ (Kaur et al.[19] p. 206). The segregation factor, s, is equal to one for self-diffusion of oxygen in oxides.

The A regime is reached after the annealing time $t_{\text{A regime}}$ if the characteristic diffusion depth into the grain is much larger than the mean grain size ($2R$) of the polycrystalline solid (Kaur et al.[19] p. 210) so that one has

$$t_{\text{A regime}} \gg \frac{4R^2}{D} \qquad (15)$$

That is, for annealing times $t > t_{\text{A regime}}$ the reduction–oxidation kinetics of a polycrystalline solid can be modelled like in Sections 2.1 and 2.2 if one replaces D by D_{eff} (defined by eqn (14)) in the corresponding equations.

2.5 Concluding remarks

In Sections 2.1 and 2.2 we mathematically modelled the reduction–oxidation process of a homogeneous solid oxide. At least two parameters determine the kinetics of this process, first, the oxygen exchange coefficient, K, at the gas/solid interface, and second, the oxygen diffusion coefficient, D, in the solid. If one assumes that these parameters depend on temperature only one can model the reduction–oxidation process analytically for different geometries of the solid (see eqn (3) and (8)). The analytical solutions allow one to define a dimensionless regime parameter $L = \xi K/D$ where ξ corresponds to a characteristic length of the solid (half the thickness of a plane sheet or the radius of a sphere, respectively). Fig. 1 shows that one can distinguish three fundamental kinetic regimes: the surface controlled regime for $L < 0.3$, the mixed regime in the parameter range $0.3 < L < 30$, and the diffusion controlled regime for $L > 30$. Because the regime parameter L is proportional to the characteristic length of the solid one will generally reach the surface controlled regime if the characteristic length of a given solid at a given temperature (fixed parameters D and K) becomes sufficiently small. That is, the ad hoc hypothesis that the kinetics is surface controlled is principally more reasonable for microscopic geometries than for macroscopic geometries.

As discussed in Section 2.3, in the whole range of the dimensionless regime parameter L one can evaluate the characteristic time constant of the reduction–oxidation process by a simple exponential decay function (eqn (13)) with practically sufficient accuracy if the mass loss/gain is monitored up to equilibrium. However, the characteristic time constant is generally, even in this

5852 | Phys. Chem. Chem. Phys., 2015, **17**, 5849–5860

This journal is © the Owner Societies 2015

simple model of two constant parameters, a complicated function of the parameters K and D (see eqn (5) and (10)). In the mixed regime one has to know one parameter to evaluate the conjugate parameter by the measured time constant. In the surface controlled regime one can evaluate K and in the diffusion controlled regime one can evaluate D. This, however, requires a correct hypothesis related to the kinetics regime as defined in Fig. 1.

In Section 2.4 we considered a polycrystalline solid. Eqn (15) allows one to estimate the time interval which is required to reach the so called A regime in which a polycrystalline solid can be mathematically modelled like a homogeneous solid. If the A regime is reached the reduction–oxidation process of a polycrystalline solid oxide can be modelled as in Sections 2.1 and 2.2 with an effective oxygen diffusion coefficient (eqn (14)).

3 Experimental

3.1 Sample preparation

CeO_2 powders were synthesized using a citric acid assisted combustion method.[22] For that the required amount of $Ce(NO_3)_3 \times 6H_2O$ (Sigma Aldrich) was dissolved in demineralized water. Afterwards citric acid (VWR chemicals) solution was added in a molar ratio of 1 : 2 (cations : citric acid) and the obtained mixture was stirred at 100 °C for 1 h. Stepwise increase of the temperature up to 200 °C resulted in a more and more concentrated solution due to water evaporation thus leading to the formation of a very viscous yellow gel. The viscous product was heated to 450 °C for self-ignition. The newly formed yellow powder was calcined in an electrical furnace at 800 °C in air for 2 h to remove any remaining carbonaceous species. The obtained oxide powder was analyzed by X-ray diffractometry (D-5000, Siemens, Germany) using Ni-filtered Cu-Kα radiation. The CaF_2-type CeO_2 phase (Fig. 4) was identified according to reference data ICDD PDF-00-034-0394.[23]

To prepare pellets the powder was milled using a laboratory ball mill [planetary micromill pulverisette 7, Fritzsch, Germany (3 × 10 min, 500 rpm, mass ratio of 1 : 10 : 60 powder: isopropyl alcohol: ZrO_2 balls)] and uniaxially cold-pressed at a pressure of 283 MPa. After sintering at 1650 °C for 2 h the pellets had a density of 93% (see Table 1). Beside X-ray diffraction the
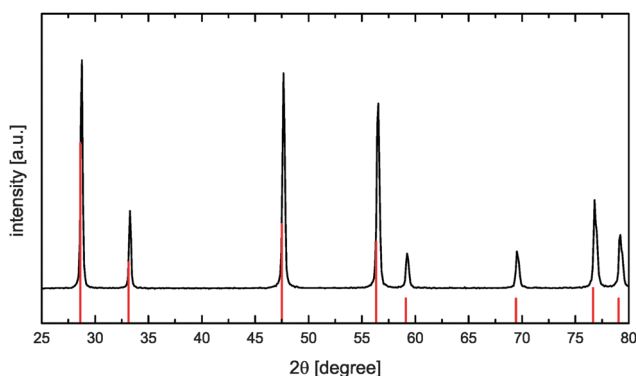
Table 1 Dimensions and density of the (fully oxidized) CeO_2 pellet used for thermogravimetric analysis

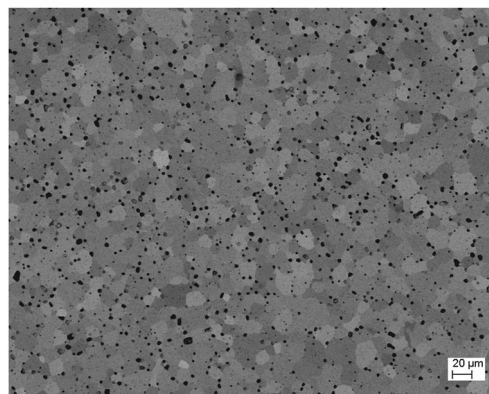| Parameter	Value
Thickness	1.05 mm
Diameter	13.44 mm
Weight	911.4 mg
Density	6.7 g cm^{-3}
Theor. density[23]	7.2 g cm^{-3}

Fig. 5 SEM image of the sintered CeO_2 pellet with a grain size of about 20 μm and a density of 93% (Angle Selective Backscatter detector).

sintered samples were characterized by scanning electron microscopy (SEM, Ultra 55 FEG Carl Zeiss, Germany) equipped with an energy-dispersive X-ray spectroscopy (EDS) system (Fig. 5 and 6). EDS analyses (INCA-Software, Oxford Instruments, Abingdon, UK, Fig. 6) revealed minor impurities of Zr of about 0.58 ± 0.03 at% (at%[Ce] + at%[Zr] + at%[O] = 100 at%) which leads to $Ce_{0.98}Zr_{0.02}O_2$. In a first approximation homovalent Zr does not act as an acceptor in ceria in such a low concentration. Therefore, we refer to our material as nominally undoped.

3.2 Thermogravimetric analysis

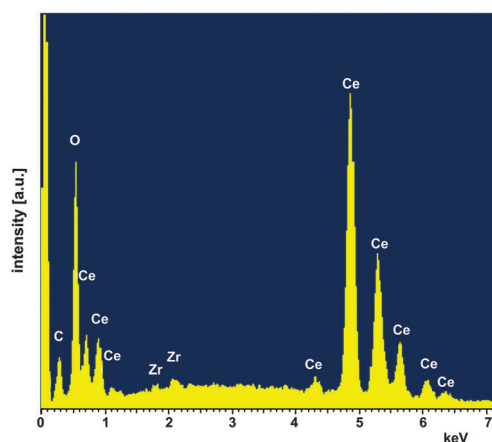Thermogravimetric (TG) analyses were performed using a thermo-balance system STA 449 F3 Jupiter (Netzsch, Germany).

Fig. 4 XRD pattern of the synthesized CeO_2 sample (reference data according to ICDD PDF-00-034-0394[23] as red solid vertical lines).

Fig. 6 EDS analysis of the sintered CeO_2 pellet.

This journal is © the Owner Societies 2015

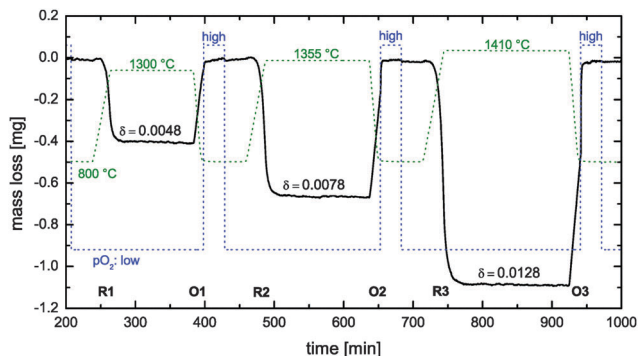*Phys. Chem. Chem. Phys.*, 2015, **17**, 5849–5860 | 5853

Fig. 7 Reduction cycles (R1–R3) und oxidation cycles (O1–O3) during thermogravimetric analysis of a nominally undoped polycrystalline CeO$_2$ pellet (see Table 1). Dashed lines show the time dependence of the temperature and the oxygen partial pressure p_{O_2} (low: 7×10^{-4} atm, high: 0.4 atm).

Fig. 8 Isothermal time dependence of the mass loss during the reduction cycles R1–R3 in Fig. 7 where m_0 is the mass at time t_0 when the temperature starts to become constant. Time constants, τ, to reach mass equilibrium are evaluated by fit eqn (13) where the R^2 values quantify the fit quality.

A sintered CeO$_2$ pellet (see Table 1) was placed on Pt foil on an Al$_2$O$_3$ plate (diameter: 13 mm). For the reduction steps (at different high temperatures with a heating rate of 20 K min^{-1}, see Fig. 7) argon 5.0 was passed through the sample tube at a flow rate of 85 ml min^{-1}. The partial pressure of the employed gas atmosphere during the reduction step was calculated to be approximately 7×10^{-4} atm by comparing the obtained suboxide compositions with literature data.[24] The reduction temperatures were held for several hours for complete reduction. For the subsequent oxidation step the pellet was rapidly cooled (50 K min^{-1}) to 800 °C. After a dwell time of 5 min at 800 °C an argon–oxygen gas mixture was employed for 30 min (35 ml min^{-1} O$_2$, 50 ml min^{-1} Ar which corresponds to an oxygen partial pressure of about 0.4 atm). Next, the gas was switched back to pure Ar 5.0 followed by a new reduction step.

For data analysis the obtained mass loss curve was corrected by subtraction of a blank run (TG measurement without sample) to minimize device artefacts. Three reduction–oxidation cycles of the CeO$_2$ pellet are shown in Fig. 7. Dashed lines show the monitored time dependence of the temperature and of the oxygen partial pressure. Oxygen nonstoichiometry, δ, of ceria was calculated by

$$\delta = -\frac{M_{CeO_2}}{M_O}\frac{\Delta m_{eq}}{m_s} \qquad (16)$$

where M is the molar mass, Δm_{eq} the equilibrium value of the mass loss during the reduction cycle and m_s the sample mass (911.4 mg) in the fully oxidized state. Because of the relatively high p_{O_2} during oxidation it was assumed $\delta = 0$ after each oxidation cycle.[25]

3.2.1 Observed reduction–oxidation kinetics. Reduction cycle #1 (see R1 in Fig. 7) was induced by increasing (20 K min^{-1}) the temperature to 1300 °C and keeping the (low) oxygen partial pressure constant. Because the reduction equilibrium is temperature dependent[7] one observes that the CeO$_2$ pellet is loosing some mass during the temperature increase. However, the time required to reach the reduction temperature is not sufficient to reach equilibrium at the reduction temperature. Therefore, one can also observe an *isothermal* mass loss which starts when the
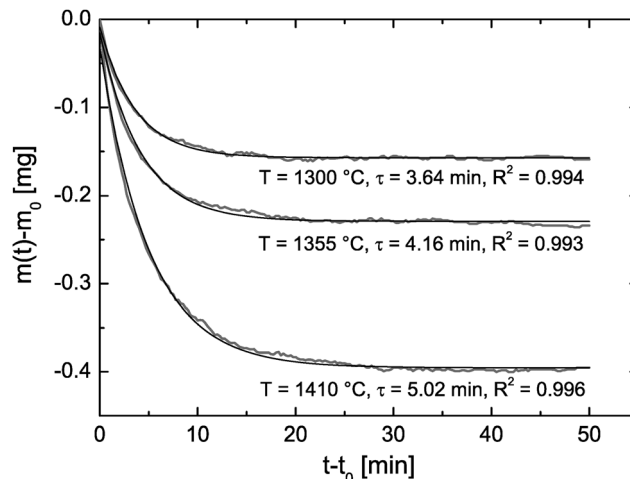
reduction temperature begins to become constant in Fig. 8. This isothermal mass loss is separately plotted in Fig. 8 for all monitored reduction cycles (reduction temperatures). Fig. 8 shows that the isothermal mass loss is well fitted by an exponential decay function (eqn (13)) so that the isothermal mass loss is well characterised by a single time constant, τ, as compiled in Table 2. The evaluated characteristic time constants are increasing for increasing reduction temperatures.

Considering oxidation cycle #1 (see O1 in Fig. 7) one observes that the CeO$_2$ pellet gains mass linearly because the oxidation kinetics is sufficiently fast to follow the linear temperature change (50 K min^{-1}). An increase of the oxygen partial pressure does not change the oxidation state because the pellet is already oxidised up to its maximum oxidation state. However, at oxidation cycles #2 and #3 the pellet does not reach its maximum oxidation state when the oxidation temperature (800 °C) is reached. One can now observe that a rapid increase of the oxygen partial pressure induces a rapid increase of the oxidation kinetics.

3.3 Oxygen isotope exchange

Considering a plane sheet the tracer diffusion coefficient, D^*, and the tracer surface exchange coefficient, K^*, of oxygen are defined by (compare with eqn (22) which defines the corresponding chemical coefficients for oxygen)

$$|j_{^{18}O}| = D^*\left(\left|\frac{\partial c_{^{18}O}}{\partial x}\right|\right)_{x=0} = K^*|c_{^{18}O}{}^g - c_{^{18}O}(x=0)| \qquad (17)$$

where $j_{^{18}O}$ is the oxygen tracer isotope (^{18}O in this work) flux through the gas/solid interface, $c_{^{18}O}{}^g$ is the concentration of the oxygen isotope in the gas phase and $c_{^{18}O}$ the actual concentration of the oxygen isotope in the solid. The analytical solution of the diffusion problem with such a boundary condition (eqn (17)) in a semi-infinite homogeneous media is given

Table 2 Computed chemical surface exchange coefficients, $\tilde{K}$, of oxygen from the time constants shown in Fig. 8 where $\lambda = \xi = 0.5$ mm. The corresponding δ values are from Fig. 7. The expected high temperature range of the chemical diffusion coefficient, $\tilde{D}$, was estimated from Fig. 1b of Ackermann et al.[8]

T (°C)	p_{O_2} (atm)	δ	τ (min)	$\tilde{K} = \lambda/\tau$ (m s^{-1})	$\tilde{D}$ (m^2 s^{-1})	$L = \xi\tilde{K}/\tilde{D}$
1300	7×10^{-4}	0.0048	3.64	2.29×10^{-6}	$10^{-7}\cdots10^{-8}$	$1.1 \times (10^{-2}\cdots10^{-1})$
1355	7×10^{-4}	0.0078	4.16	2.00×10^{-6}	$10^{-7}\cdots10^{-8}$	$1.0 \times (10^{-2}\cdots10^{-1})$
1410	7×10^{-4}	0.0128	5.02	1.66×10^{-6}	$10^{-7}\cdots10^{-8}$	$8.3 \times (10^{-3}\cdots10^{-2})$

by Crank[15] (the special notation of the solution was proposed by Fielitz and Borchardt[26])

$$\frac{c_{^{18}O}(x,t)-c_{^{18}O}^{\infty}}{c_{^{18}O}^{g}-c_{^{18}O}^{\infty}} = \operatorname{erfc}\left(\frac{x}{\sigma^*}\right) - \exp\left(2\frac{x}{\sigma^*}\sqrt{\frac{t}{\tau^*}}+\frac{t}{\tau^*}\right)\operatorname{erfc}\left(\frac{x}{\sigma^*}+\sqrt{\frac{t}{\tau^*}}\right)$$

$$\text{with } \sigma^* \equiv 2\sqrt{D^*t} \text{ and } \tau^* \equiv \frac{D^*}{K^{*2}}$$

$$(18)$$

where $c_{^{18}O}^{\infty}$ is the natural abundance of ^{18}O in the sample (at $x \to \infty$), σ^* is the diffusion length of the tracer isotope and τ^* the characteristic time constant to reach tracer isotope equilibrium at the gas/solid interface.

D^* and K^* data measured by ^{18}O tracer exchange experiments in nominally undoped CeO$_2$ ceramics are already available in the literature.[3] Furthermore, tracer coefficients (D^*,K^*) are not directly applicable to rationalise the features of the reduction–oxidation kinetics during thermogravimetric analysis because the observed kinetics is controlled by chemical coefficients $(\tilde{D},\tilde{K})$ which generally differ significantly from tracer coefficients.[11] Nevertheless, it was useful to perform also an ^{18}O tracer exchange experiment because in Section 4.1 we will discuss that fast diffusion paths in CeO$_2$ ceramics support the hypothesis that the observed reduction–oxidation kinetics during thermogravimetric analysis is surface controlled. That is, it was in the context of this work interesting to confirm, at least qualitatively, such fast diffusion paths by an ^{18}O exchange experiment.

Fig. 9 shows SIMS depth profiles measured in a nominally undoped polycrystalline CeO$_2$ sample (93% of theoretical density with an average grain size of about 20 μm) which was annealed

for 900 s in 200 mbar $^{18}O_2$ gas (96% atomic fraction) at 700 °C. The sample was pre-annealed for 3 hours in 200 mbar $^{16}O_2$ at 700 °C. Fig. 9a shows SIMS raw data of the depth distribution of the negative secondary ions $^{16}O^-$, $^{18}O^-$, $^{140}Ce^-$ using a Hiden Analytical instrument. Positive 5 keV argon ions were used as primary beam with 400 nA ion current and a spot size of about 60 μm. The raster-scanned area was 450×350 μm^2 and the area of the analysed zone was 170×130 μm^2. Negative secondary ions were used for the analysis of the samples. Sample charging was prevented by an electron flood gun. Depth calibration was done by measuring the SIMS crater depth using a surface profiler (Tencor, Alpha Step 500). Differences in sputter yield and ionisation yield can be neglected for isotopes so that the depth distribution of the atomic fraction of ^{18}O isotopes can be quantified by

$$c_{^{18}O} = \frac{I(^{18}O)}{I(^{18}O)+I(^{16}O)}$$

$$(19)$$

from the raw data, where I is the intensity of the SIMS signal.

The depth distribution of the atomic fraction of ^{18}O isotopes is shown in Fig. 9b. One can see that the atomic fraction of ^{18}O in the sample at $x = 0$ does not yet reach the atomic fraction of ^{18}O of the gas phase (96%) which clearly indicates a tracer surface exchange coefficient, K^*, which is sufficiently low to prevent tracer isotope equilibrium at the gas/solid interface during the annealing time $t = 900$ s at 700 °C. The most interesting feature of this depth profile, in the context of this work, is the significant tail (above the natural abundance of ^{18}O) which clearly indicates (at least qualitatively) the existence of fast diffusion paths in the CeO$_2$ samples investigated. The ^{18}O tracer coefficients (K^*,D^*) were evaluated using
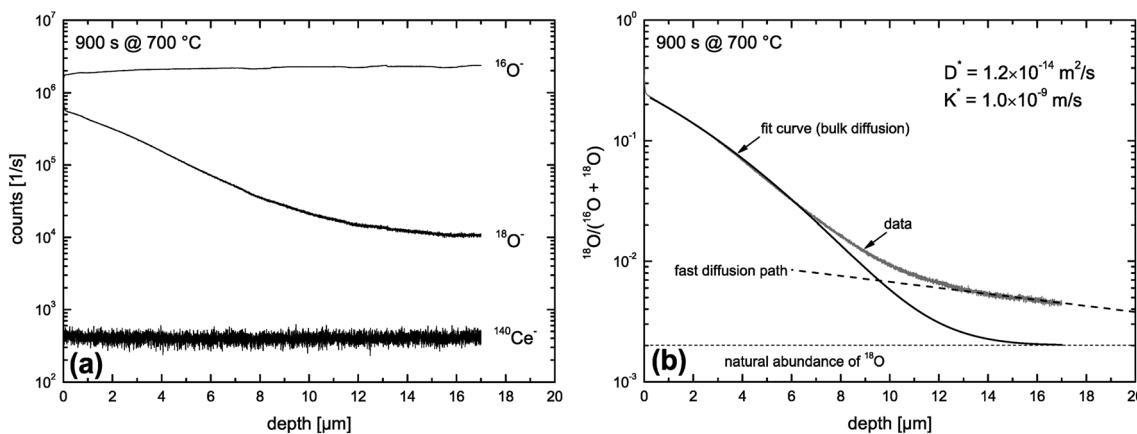

Fig. 9 SIMS depth profiles measured in a nominally undoped polycrystalline CeO$_2$ sample which was annealed for 900 s in 200 mbar $^{18}O_2$ gas at 700 °C. (a) SIMS raw data. (b) Atomic fraction of ^{18}O computed by eqn (19).

eqn (18) as fit equation and are plotted in Fig. 10. From these data one can estimate that the characteristic time constant to reach tracer isotope equilibrium at the gas/solid interface is $\tau^* = D^*/K^{*2} = 12\,000$ s at 700 °C.

4 Discussion

The features of the observed reduction–oxidation kinetics during thermogravimetric analysis of nominally undoped poly-crystalline CeO$_2$ (93% density) are summarized in Section 3.2.1. Before one tries to rationalise these observed features one must first make a correct decision concerning the kinetics regime. This will be facilitated by an estimation of the kinetics regime during oxygen tracer exchange.

4.1 Estimation of conditions to reach the surface controlled regime during oxygen tracer exchange

As discussed in Section 2.5 one can principally expect that the observed kinetics becomes surface controlled for sufficiently small grains. This principal conclusion is supported by an experimental work of Rutman et al.[10] where SIMS analysis and combined residual gas analysis of nano crystals (5 to 50 nm size) of CeO$_2$ + 10%Gd$_2$O$_3$ were used to measure tracer surface exchange and tracer diffusion of oxygen at low temperatures, 337 °C ≤ T ≤ 461 °C. However, isotope surface exchange was found to be the limiting step and solely K^* could be determined from the performed tracer exchange experiments.

The CeO$_2$ grains in the sintered nominally undoped samples of this work have an average size of about 20 μm. The question arises whether reactions on individual isolated crystals of this size are surface controlled at temperatures used during the reduction step of the thermogravimetric analysis ($T \geq 1300$ °C). That is, we first ask what we can expect if we use CeO$_2$ powder (crystals of about 20 μm

size) instead of sintered ceramics. To get an estimation we consider D^* and K^* data measured by ^{18}O tracer exchange experiments in nominally undoped CeO$_2$ (Kamiya et al.[3] and this work) which are plotted in Fig. 10a. The left hand axis of Fig. 10b shows the corresponding ratios K^*/D^*. To evaluate whether small grains are surface controlled during an oxygen tracer exchange one has to consider the regime parameter $L = R \cdot K^*/D^*$ which indicates a surface controlled regime for values $L < 0.3$ (see Fig. 1). The regime parameter L is plotted on the right hand axis of Fig. 10b for grains of $R = 10$ μm. This clearly indicates that the oxygen tracer exchange kinetics of small grains of Gd doped CeO$_2$ (GDC) is surface controlled in the whole temperature range because the ratio K^*/D^* tends to become temperature independent at higher temperatures.[2] (To show that this tendency is not accidental also K^*/D^* values of Y doped ZrO$_2$ are plotted.[2])

After we have seen that the oxygen tracer exchange for small grains ($R = 10$ μm) of GDC is clearly surface controlled we will answer the question whether a thin dense polycrystalline plane sheet of GDC could also be surface controlled. For that we consider a plane sheet of dense polycrystalline GDC of 1 mm thickness ($\xi = 0.5$ mm = half the thickness) with an average grain radius $R = 10$ μm. At $T > 600$ °C grain boundary blocking effects vanish in GDC[27] so that one can describe the oxygen tracer transport in fine-grained polycrystalline GDC by an effective diffusion coefficient D_{eff}^* as discussed in Section 2.4. That is, the (surface controlled) regime of polycrystalline GDC will not change if the following equation holds (see Fig. 10b where $L \leq 0.01$ for GDC)

$$\frac{\xi}{D_{\text{eff}}^*}K^* \approx \frac{R}{D^*}K^* = L \leq 0.01 \quad \text{if} \quad R = 10\,\mu\text{m} \tag{20}$$

so that one has (considering eqn (14) with $s = 1$)

$$\frac{\xi}{R} = \frac{0.5\text{ mm}}{10\,\mu\text{m}} = 50 \approx \frac{D_{\text{eff}}^*}{D^*} = g\frac{D_{\text{gb}}^*}{D^*} + (1-g) \tag{21}$$
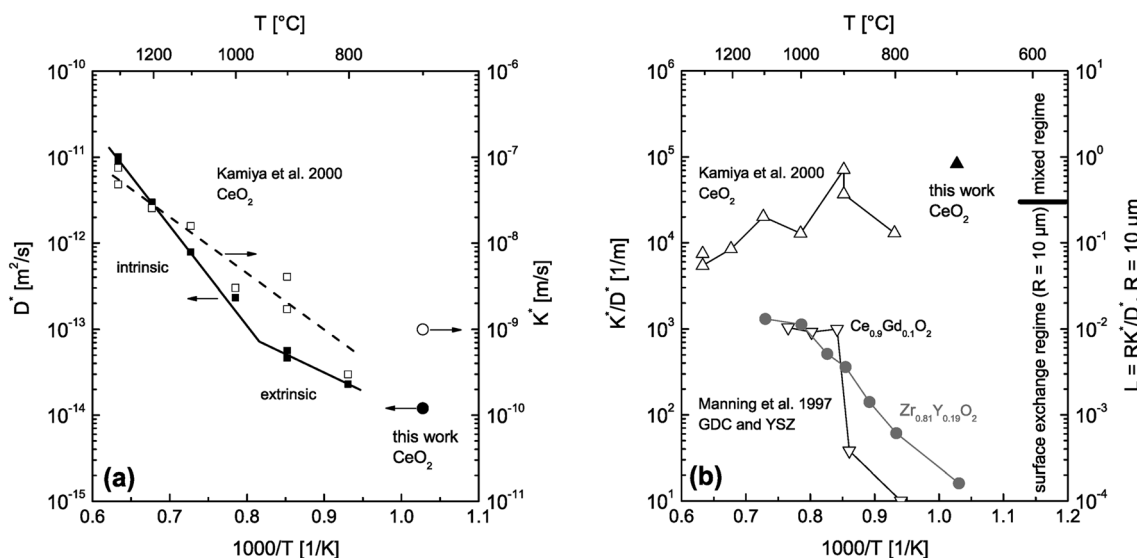

Fig. 10 (a) D^* and K^* data measured by ^{18}O tracer exchange experiments in nominally undoped polycrystalline CeO$_2$ (Kamiya et al.[3] and this work). (b) calculated K^*/D^* values from the data of (a). For comparison K^*/D^* values are also shown for Gd doped CeO$_2$ (GDC) and Y doped ZrO$_2$ (YSZ).[2] The regime parameter $L = R \cdot K^*/D^*$ was calculated for grains of $R = 10$ μm and shows which material can be expected to be surface controlled in which temperature range.

5856 | *Phys. Chem. Chem. Phys.*, 2015, **17**, 5849–5860

This journal is © the Owner Societies 2015

where g is the volume fraction of grain boundaries and D_{gb}^* the tracer diffusion coefficient of oxygen in the grain boundaries. A ratio of $D_{gb}^*/D^* \approx 10^4$ for the oxygen tracer diffusivities in polycrystalline mullite ceramics has been reported.[28] Assuming a similar ratio a value $g \approx 0.5\%$ would be sufficient to ensure a surface controlled regime. Simplifying the real grain structure by cubic grains ($q = 3$) a value $g = q\omega/(2R) \approx 0.5\%$ requires, however, an unrealistic grain boundary width of $\omega \approx 33$ nm to ensure a regime parameter of $L \leq 0.01$ ($\omega \approx 1$ nm was assumed by Fielitz et al.[28]). A more realistic average grain boundary width of $\omega \approx 3$ nm shifts the regime parameter to $L \leq 0.1$ so that the kinetics regime remains surface controlled also for a plane sheet (1 mm thickness, average grain radius $R = 10$ μm) of polycrystalline dense GDC if $D_{gb}^*/D^* \approx 10^4$. Unfortunately, there are no grain boundary oxygen tracer diffusion coefficients, D_{gb}^*, available in the literature for GDC to quantify this discussion. Nevertheless, it demonstrates that a surface controlled kinetics regime is not unrealistic even for *dense* polycrystalline GDC of 1 mm thickness. Strictly speaking, the details of the physical nature of the rapid diffusion paths are not important as long as the effective diffusion in the bulk is fast enough to yield $L < 0.3$. For example, if one assumes that the porosity of about 7% (see Table 1) is essentially an open one and consists of pores in the diameter range 1 to 5 μm and a specific total pore cross section of about 20 μm² per grain (grain size = 20 μm) the resulting Knudson diffusivity, D_K, of oxygen molecules would fall into an interval 10^{-4} m² s⁻¹ $\leq D_K$ (1 bar, 1300 °C) $\leq 10^{-3}$ m² s⁻¹ which is much more rapid than any realistic estimate of D_{gb}^* from the D^* values published for GDC (see Kamiya et al.[3]). In reality, for small values of the porosity, both diffusion in the pores and in the grain boundaries will contribute to the enhanced oxygen transport in the material.

The situation is different for nominally undoped CeO₂ (as used in this work) because the oxygen tracer exchange kinetics of small grains ($R = 10$ μm) tends to be in the mixed regime at lower temperatures and tends to be in the surface controlled regime at higher temperatures (see Fig. 10b). The reason that small grains of GDC are clearly in the surface controlled regime is that the oxygen diffusivity in the grains is increased significantly by Gd doping compared to nominally undoped CeO₂.[3] The Gd doping increases the concentration of oxygen vacancies, and hence, the diffusivity of oxygen which is assumed to be based on a vacancy mechanism.[3]

Furthermore, one has to keep in mind that the measured D^* and K^* data represent CeO₂ samples which were pre-annealed in air[3] (200 mbar ¹⁶O₂ gas in this work), and hence, in a highly oxidized state during the ¹⁸O exchange experiments. Fig. 10b indicates that even highly oxidized CeO₂ grains tend to reach the surface controlled regime at high temperatures, $T \geq 1300$ °C, if the radius of the CeO₂ grains is about 10 μm. As the reduction of nominally undoped ceria increases the vacancy concentration and thus the oxygen diffusivity one can conclude that a surface controlled regime is also plausible for nominally undoped polycrystalline CeO₂ of 1 mm thickness (93% density). This argument and the fact that one can generally expect much higher chemical oxygen diffusion coefficients than tracer oxygen diffusions coefficients[11] suggests a surface controlled kinetics regime for the polycrystalline ceria sample used in this work during TG analysis, which will be discussed in the next section.

4.2 Reduction kinetics of CeO₂ in the surface controlled regime

We now postulate that the observed reduction kinetics during the performed thermogravimetric analysis (see Fig. 7) is surface controlled. This *ad hoc* hypothesis is motivated by the above discussion of oxygen *tracer* diffusion data and will be supported if it allows one to rationalise the observed features of the kinetics summarized in Section 3.2.1.

Considering a plane sheet the chemical diffusion coefficient, $\tilde{D}$, and the chemical surface exchange coefficient, $\tilde{K}$, of oxygen are defined by (compare with eqn (17) which defines the corresponding tracer coefficients for oxygen)

$$|j_O| = \tilde{D}\left(\left|\frac{\partial c_O}{\partial x}\right|\right)_{x=0} = \tilde{K}\left|c_O^{eq} - c_O(x=0)\right| \qquad (22)$$

where j_O is the oxygen flux through the gas/solid interface, c_O^{eq} is the equilibrium and c_O the actual concentration of oxygen in the solid. In the surface controlled regime the observed kinetics of an isothermal mass change (induced by oxygen loss/gain) is given by (see eqn (6) and (11))

$$\left|\frac{m(t) - m_0}{m_\infty - m_0}\right| = 1 - \exp\left(-\frac{t - t_0}{\tau}\right) \quad \text{with} \quad \tau = \frac{\lambda}{\tilde{K}} \qquad (23)$$

where m_0 is the mass of the solid at $t = t_0$, m_∞ is the equilibrium mass of the solid (at $t = \infty$), τ is the observed time constant and λ a characteristic length of the solid ($\lambda = R/3$ for a sphere of radius R and $\lambda = h/2$ for a plane sheet of thickness h).

In Table 2 chemical surface exchange coefficients, $\tilde{K}$, of oxygen are computed with the aid of eqn (23) from the time constants evaluated from the isothermal mass loss in Fig. 8 where $\lambda = 0.5$ mm. The expected range of the chemical diffusion coefficient, $\tilde{D}$, in the considered temperature range was estimated from Fig. 1b of Ackermann et al.[8] so that also the expected range of the corresponding regime parameter L is computed in Table 2. The range of L is for all three temperatures less than 0.3 which supports the *ad hoc* hypothesis of a surface controlled kinetics regime (see Fig. 1).

If one compares the chemical surface exchange coefficients, $\tilde{K}$, in Table 2 with the tracer surface exchange coefficients, K^*, in Fig. 10 one finds that $\tilde{K}$ is about one order of magnitude larger than K^* at 1300 °C which is due to the average thermodynamic factor: a straightforward calculation using the data published by Panlener et al.[25] shows that it varies between $60\cdots500$ for $0.2 \geq \delta \geq 0.03$ and that it is virtually independent of temperature. This is in accordance with the general observation $\tilde{K} \gg K^*$.[11] Furthermore, there is a surprising temperature dependence of the evaluated chemical surface exchange coefficient, $\tilde{K}$. It decreases with temperature which is in contrast to the tracer surface exchange coefficients, K^*, which increases with temperature (see Fig. 10). From the data of Table 2 one can evaluate the following Arrhenius relation for the chemical surface exchange coefficient of nominally undoped CeO₂ (at $p_{O_2} = 7 \times 10^{-4}$ atm)

$$\tilde{K} = \left(1.7^{+1.2}_{-0.7}\right) \times 10^{-8}\frac{m}{s}\exp\left(\frac{(64 \pm 7)\,\text{kJ mol}^{-1}}{RT}\right) \qquad (24)$$

This journal is © the Owner Societies 2015

Phys. Chem. Chem. Phys., 2015, **17**, 5849–5860 | 5857

Note the negative apparent activation energy in eqn (24). Its absolute value in common units is (64 ± 7) kJ mol^{-1} or (0.67 ± 0.07) eV at^{-1}, respectively.

Considering Table 2 one notes that there is an empirical relation, $\tilde{K} \sim \delta^{-0.32}$, between the chemical surface exchange coefficient and the oxygen nonstoichiometry. Because δ is approximately equal to the concentration of vacancies in nominally undoped CeO$_2$ one can conclude that $\tilde{K} \sim [V_O^{\bullet\bullet}]^{-0.32}$. Please note that our data analysis assumed that $\tilde{K}$ is a constant so that eqn (23) is not exact as $\tilde{K} = \tilde{K}(\delta)$. However, the assumption $\tilde{K} \approx$ const. is reasonable if δ is close to the equilibrium value, $\delta \approx \delta_{eq}$, which was approximately the case for the isothermal mass loss curves considered in Fig. 8. Furthermore, if one considers the oxidation cycles in Fig. 7 the "jump" of the oxidation rate, which is induced by a "jump" of the oxygen partial pressure, can immediately be rationalised if one sets $\tilde{K} \sim p_{O_2}^{1/n}$. The relation $K^* \sim p_{O_2}^{1/4}$ has been reported for the tracer exchange coefficient in polycrystalline Gd doped CeO$_2$.[29]

Summarising, the observed kinetics (see Section 3.2.1) during TG analysis of nominally undoped ceria can be empirically rationalised if the chemical oxygen surface exchange coefficient obeys the following relation

$$\tilde{K} = \tilde{k} \frac{p_{O_2}^{1/n}}{[V_O^{\bullet\bullet}]^{1/m}} \qquad (25)$$

where $\tilde{k} = \tilde{k}(T)$ is a temperature dependent constant of proportionality.[12] A value of $m \approx 3$ is estimated from the data for $\tilde{K}$ in Table 2. For the oxygen tracer surface exchange coefficient of acceptor-doped perovskite and fluorite oxides the empirical relation $K^* = k^* p_{O_2}^{1/4} [V_O^{\bullet\bullet}]^{-1/2}$ has been reported.[12] That is, the assumption that $n \approx 4$ in eqn (25) is, at least, a good starting assumption if one tries to confirm eqn (25) quantitatively by future investigations. In this work it was not possible to estimate n in eqn (25) because the oxygen partial pressure was rapidly switched in only one step (from low values to high values or in the opposite direction) and because the response of the mass change was too rapid to be detected reliably (see Fig. 7).

From eqn (25) one concludes that the negative apparent activation energy of the chemical surface exchange coefficient, $\tilde{K}$, is given by

$$\Delta E_a^{\tilde{K}} = \Delta E_a^{\tilde{k}} - \frac{1}{m} \Delta E_a^{V_O^{\bullet\bullet}} = -64 \text{ kJ mol}^{-1} \qquad (26)$$

so that one has to quantify $\Delta E_a^{\tilde{k}}$ and $\Delta E_a^{V_O^{\bullet\bullet}}$ in this equation. The latter parameter can be identified as the formation energy of oxygen vacancies in nominally undoped CeO$_2$. For this quantity, Kamiya et al.[3] found 142 kJ mol^{-1}, which is close to the value given by Panhans and Blumenthal,[30] 152 kJ mol^{-1}. Inserting the average value of 147 kJ mol^{-1} for $\Delta E_a^{V_O^{\bullet\bullet}}$ into eqn (26) one gets for $m \approx 3$ the negative apparent activation energy $\Delta E_a^{\tilde{k}} \approx -15$ kJ mol^{-1}. Due to the typical errors of experimentally determined energies of activation this value is in fact close to zero and should be observed if the formation energy of oxygen vacancies is negligible. A negligible formation energy of oxygen vacancies can be expected in Gd doped CeO$_2$

(GDC) during oxygen tracer exchange experiments because Gd doping forms temperature independent oxygen vacancies according to the reaction

$$Gd_2O_3 + 2Ce_{Ce} + O_O \rightarrow 2Gd_{Ce}' + V_O^{\bullet\bullet} + 2CeO_2 \qquad (27)$$

Armstrong et al.[6] reported an apparent activation energy $\Delta E_a^{K^*} = 3$ kJ mol^{-1} for the oxygen tracer surface exchange coefficient, K^*, of GDC. Their experimental method is based on rapid switching of the reactor/furnace feed line between gas streams containing different isotopes of oxygen (^{18}O, ^{16}O) which are monitored by a mass spectrometer.[31] Ideally, the only change induced by the switch is a step in oxygen labelling. Temperature, pressure, flow rate, and oxygen partial pressure remain approximately undisturbed. Because powders of the investigated oxides were used (size <1 μm) it was assumed that the oxygen isotope exchange kinetics is surface controlled.

Interestingly enough Armstrong et al.[13] recently reported apparent activation energies of K^* for different perovskite oxides which have also negative or very small positive values. The reported range of apparent activation energies, $\Delta E_a^{K^*}$, of the oxygen tracer surface exchange coefficient is -97 kJ mol$^{-1} \leq \Delta E_a^{K^*} \leq +12$ kJ mol^{-1} (see Armstrong et al.[13] Table 5). Armstrong et al.[13] assume that such small, and even negative, apparent activation energies indicate a surface exchange controlled kinetics regime. On the contrary, reported apparent activation energies from SIMS isotope depth profiles or electrical conductivity relaxation are typically measured in the mixed kinetics regime and have much larger positive values (73 kJ mol^{-1} to 333 kJ mol^{-1}, see Armstrong et al.[13] Table 5). The reason is yet unclear why the measured value of the apparent activation energy of the oxygen surface exchange coefficient depends on the kinetics regime.

5. Conclusions

In Section 3.2.1 the observed features of the reduction–oxidation kinetics during thermogravimetric analysis of nominally undoped CeO$_2$ ceramics are summarized. Before one tries to rationalise these observed features one needs a correct *ad hoc* hypothesis concerning the kinetics regime (surface controlled kinetics, mixed kinetics, diffusion controlled kinetics, as shown in Fig. 1). The most important parameter to estimate quantitatively the correct kinetics regime is the dimensionless regime parameter, $L = \xi \cdot \tilde{K}/\tilde{D}$, where ξ is half the thickness of a plane sheet or the radius of a sphere, respectively. The problem is, however, that *both chemical* coefficients ($\tilde{K}, \tilde{D}$) are often not available in the literature so that one must consider measured tracer coefficients (K^*, D^*) together with the thermodynamic factor (if available). As discussed in Section 4.1. measured tracer coefficients of nominally undoped and Gd doped CeO$_2$ suggested the hypothesis that the observed reduction–oxidation kinetics during the performed thermogravimetric analysis is surface controlled for dense polycrystalline samples of 1 mm thickness and 20 μm grain size–especially, if one takes into account that chemical oxygen diffusion coefficients are generally observed to be much larger than oxygen tracer diffusion coefficients.[11]

5858 | *Phys. Chem. Chem. Phys.*, 2015, **17**, 5849–5860

This journal is © the Owner Societies 2015

Further, the effective oxygen diffusivity can be significantly enhanced due to grain boundary transport.

In Section 4.2 we postulated a surface controlled kinetics regime during the performed thermogravimetric analysis (see Fig. 7) of the sintered nominally undoped CeO_2 pellet (see Table 1). This *ad hoc* hypothesis allowed us to evaluate chemical oxygen surface exchange coefficients, $\tilde{K}$, as compiled in Table 2, from the observed isothermal reduction kinetics. The chemical oxygen surface exchange coefficients empirically obey a relation expressed by eqn (25). Considering chemical oxygen diffusion coefficients, $\tilde{D}$, from the literature (see Table 2) our *ad hoc* hypothesis is supported because the computed regime parameters, L, indicates a surface exchange regime. This finding is an important design criterion for an efficient microstructure of the ceria inventory of a solar-thermal splitting reactor.

The observed negative apparent activation energy, $\Delta E_a^{\tilde{K}} = -64$ kJ mol^{-1}, of the chemical oxygen surface exchange coefficient, $\tilde{K}$, is in the range of apparent activation energies of the oxygen tracer surface exchange coefficient, K^*, for different perovskite oxides.[13] Considering reported formation energies of oxygen vacancies in nominally undoped CeO_2,[3,30] one can conclude that the apparent activation energy becomes approximately zero if the formation energy of oxygen vacancies becomes negligible as, *e.g.*, in Gd doped CeO_2. Armstrong *et al.*[6] reported an in fact negligible value for the apparent activation energy $\left(\Delta E_a^{K^*} = 3 \text{ kJ mol}^{-1} \right)$ for the oxygen tracer surface exchange coefficient, K^*, of GDC.

Appendix A

If $\cot \beta_1$ is expressed as an infinite series[32]

$$1 - L = \beta_1 \cot \beta_1 = 1 - \frac{\beta_1^2}{3} - \frac{\beta_1^4}{45} - \dots \quad \text{if} \quad |\beta_1| < \pi \quad \text{(A1)}$$

one can conclude

$$L = \frac{\beta_1^2}{3} \quad \text{if} \quad \beta_1 \to 0 \quad \text{(A2)}$$

Combining equations (A2) and (4) one gets eqn (6). Analogously, one can express $\tan\beta_1$ as an infinite series[32]

$$L = \beta_1 \tan \beta_1 = \beta_1^2 + \frac{\beta_1^4}{3} + \dots \quad \text{if} \quad |\beta_1| < \frac{\pi}{2} \quad \text{(A3)}$$

so that one has

$$L = \beta_1^2 \quad \text{if} \quad \beta_1 \to 0 \quad \text{(A4)}$$

Combining equations (A4) and (9) one gets eqn (11).

Acknowledgements

References

1 J. R. Scheffe and A. Steinfeld, Thermodynamic Analysis of Cerium-Based Oxides for Solar Thermochemical Fuel Production, *Energy Fuels*, 2012, **26**, 1928–1936.

2 P. S. Manning, J. D. Sirman and J. A. Kilner, Oxygen self-diffusion and surface exchange studies of oxide electrolytes having the fluorite structure, *Solid State Ionics*, 1997, **93**, 125–132.

3 M. Kamiya, E. Shimada, Y. Ikuma, M. Komatsu and H. Haneda, Intrinsic and Extrinsic Oxygen Diffusion and Surface Exchange Reaction in Cerium Oxide, *J. Electrochem. Soc.*, 2000, **147**, 1222–1227.

4 M. Katsuki, S. Wang, K. Yasumoto and M. Dokiya, The oxygen transport in Gd-doped ceria, *Solid State Ionics*, 2002, **154–155**, 589–595.

5 M. Stan, Y. T. Zhu and H. Jiang, Kinetics of oxygen removal from ceria, *J. Appl. Phys.*, 2004, **95**, 3358–3361.

6 E. N. Armstrong, K. L. Duncan, D. J. Oh, J. F. Weaver and E. D. Wachsman, Determination of Surface Exchange Coefficients of LSM, LSCF, YSZ, GDC Constituent Materials in Composite SOFC Cathodes, *J. Electrochem. Soc.*, 2011, **158**, B492–B499.

7 B. Bulfin, A. J. Lowe, K. A. Keogh, B. E. Murphy, O. Lübben, S. A. Krasnikov and I. V. Shvets, Analytical Model of CeO_2 Oxidation and Reduction, *J. Phys. Chem. C*, 2013, **117**, 24129–24137.

8 S. Ackermann, J. R. Scheffe and A. Steinfeld, Diffusion of Oxygen in Ceria at Elevated Temperatures and Its Application to H_2O/CO_2 Splitting Thermochemical Redox Cycles, *J. Phys. Chem. C*, 2014, **118**, 5216–5225.

9 C. B. Gopal and S. M. Haile, An electrical conductivity relaxation study of oxygen transport in samarium doped ceria, *J. Mater. Chem. A*, 2014, **2**, 2405–2417.

10 J. Rutman, M. Kilo, S. Weber and I. Riess, Tracer surface exchange and diffusion of oxygen in nano crystals of Gd doped CeO_2, *Solid State Ionics*, 2014, **265**, 29–37.

11 J. Maier, On the correlation of macroscopic and microscopic rate constants in solid state chemistry, *Solid State Ionics*, 1998, **112**, 197–228.

12 R. A. De Souza, A universal empirical expression for the isotope surface exchange coefficients (k^*) of acceptor-doped perovskite and fluorite oxides, *Phys. Chem. Chem. Phys.*, 2006, **8**, 890–897.

13 E. N. Armstrong, K. L. Duncan and E. D. Wachsman, Effect of A and B-site cations on surface exchange coefficient for ABO_3 perovskite materials, *Phys. Chem. Chem. Phys.*, 2013, **15**, 2298–2308.

14 P. J. Gellings and H. J. M. Bouwmeester, *The CRC handbook of solid state electrochemistry*, CRC Press, 1997.

15 J. Crank, *The Mathematics of Diffusion*, Oxford University Press, 2nd edn, 1975.

This journal is © the Owner Societies 2015

Phys. Chem. Chem. Phys., 2015, **17**, 5849–5860 | 5859

16 H. S. Carslaw and J. C. Jaeger, *Conduction of Heat in Solids*, Clarendon Press, 2nd edn, 1959.

17 H. Dünwald and C. Wagner, Methodik der Messung der Diffusionsgeschwindigkeiten bei Lösungsvorgängen von Gasen in festen Phasen, *Z. Phys. Chem.*, 1934, **B24**, 53–58.

18 E. Fischer and J. L. Hertz, Measurability of the diffusion and surface exchange coefficients using isotope exchange with thin film and traditional samples, *Solid State Ionics*, 2012, **218**, 18–24.

19 I. Kaur, Y. Mishin and W. Gust, *Fundamentals of Grain and Interphase Boundary Diffusion*, John Wiley & Sons Ltd, 1995.

20 E. W. Hart, On the role of dislocations in bulk diffusion, *Acta Metall.*, 1957, **5**, 597.

21 A. J. Mortlock, The effect of segregation on the solute diffusion enhancement due to the presence of dislocations, *Acta Metall.*, 1960, **8**, 132–134.

22 Q.-L. Meng, C.-i. Lee, T. Ishihara, H. Kaneko and Y. Tamaura, Reactivity of CeO_2-based ceramics for solar hydrogen production *via* a two-step water-splitting cycle with concentrated solar energy, *Int. J. Hydrogen Energy*, 2011, **36**, 13435–13441.

23 *Powder Diffraction File*, International Center for Diffraction Data (ICDD), Newtown Square, PA 19073-3273, U.S.A.

24 I. Ermanoski, N. P. Siegel and E. B. Stechel, A New Reactor Concept for Efficient Solar-Thermochemical Fuel Production, *J. Sol. Energy Eng.*, 2013, **135**, 031002.

25 R. J. Panlener, R. N. Blumenthal and J. E. Garnier, A Thermodynamic Study of Nonstoichiometric Cerium Dioxide, *J. Phys. Chem. Solids*, 1975, **36**, 1213–1222.

26 P. Fielitz and G. Borchardt, On the accurate measurement of oxygen self-diffusivities and surface exchange coefficients in oxides *via* SIMS depth profiling, *Solid State Ionics*, 2001, **144**, 71–80.

27 X.-D. Zhou, W. Huebner, I. Kosacki and H. U. Anderson, Microstructure and Grain-Boundary Effect on Electrical Properties of Gadolinium-Doped Ceria, *J. Am. Ceram. Soc.*, 2002, **85**, 1757–1762.

28 P. Fielitz, G. Borchardt, M. Schmücker, H. Schneider and P. Willich, Oxygen Grain-Boundary Diffusion in Polycrystalline Mullite Ceramics, *J. Am. Ceram. Soc.*, 2004, **87**, 2232–2236.

29 J. A. Lane and J. A. Kilner, Oxygen surface exchange on gadolinia doped ceria, *Solid State Ionics*, 2000, **136–137**, 927–932.

30 M. A. Panhans and R. N. Blumenthal, A thermodynamic and electrical conductivity study of nonstoichiometric cerium dioxide, *Solid State Ionics*, 1993, **60**, 279–298.

31 C. C. Kan, H. H. Kan, F. M. Van Assche IV, E. N. Armstrong and E. D. Wachsman, Investigating Oxygen Surface Exchange Kinetics of $La_{0.8}Sr_{.20}MnO_{3-\delta}$ and $La_{0.6}Sr_{0.4}Co_{0.2}Fe_{0.8}O_{3-\delta}$ Using an Isotopic Tracer, *J. Electrochem. Soc.*, 2008, **155**, B985–B993.

32 M. Abramowitz and I. A. Stegun, *Handbook of Mathematical Functions*, Dover Publications, 1972.

5860 | *Phys. Chem. Chem. Phys.*, 2015, **17**, 5849–5860

This journal is © the Owner Societies 2015